PCCP

PAPER

View Article Online
View Journal | View Issue

Cite this: *Phys. Chem. Chem. Phys.*, 2015, **17**, 21912

Crystallographic transformation of limestone during calcination under CO_2

Jose Manuel Valverde*[a] and Santiago Medina[b]

The calcination reaction of limestone ($CaCO_3$) to yield lime (CaO) is at the heart of many industrial applications as well as natural processes. In the recently emerged calcium-looping technology, CO_2 capture is accomplished by the carbonation of CaO in a gas–solid reactor (carbonator). CaO is derived by the calcination of limestone in a calciner reactor under necessarily high CO_2 partial pressure and high temperature. *In situ* X-ray diffraction (XRD) has been employed in this work to gain further insight into the crystallographic transformation that takes place during the calcination of limestone under CO_2, at partial pressures (P) close to the equilibrium pressure (P_{eq}) and at high temperature. Calcination under these conditions becomes extremely slow. The *in situ* XRD analysis presented here suggests the presence of an intermediate metastable CaO* phase stemming from the parent $CaCO_3$ structure. According to the reaction mechanism proposed elsewhere, the exothermicity of the CaO* → CaO transformation and high values of P/P_{eq} inhibit the nucleation of CaO at high temperatures. The wt% of CaO* remains at a relatively high level during slow calcination. Two diverse stages have been identified in the evolution of CaO crystallite size, L. Initially, L increases with $CaCO_3$ conversion, following a logarithmic law. Slow calcination allows the crystallite size to grow up from a few nanometers at nucleation up to around 100 nm near the end of conversion. Otherwise, quick calcination at relatively lower CO_2 concentrations limits CaO crystallite growth. Once calcination reaches an advanced state, the presence of CaO* drops to zero and the rate of increase of the CaO crystallite size is significantly hindered. Arguably, the first stage in CaO crystallite growth is driven by aggregation of the metastable CaO* nanocrystals, due to surface attractive forces, whereas the second one is consistent with sintering of the aggregated CaO crystals, and persists with time after full calcination is attained. Our analysis shows that the main mechanism responsible for the increase of CaO crystallite size (and thus for undermining the reactivity of the CaO) under high CO_2 partial pressure is enhanced aggregation, whereas CaO sintering is relatively less relevant, as would be expected for calcination temperatures well below the Tamman temperature.

Received 11th May 2015,
Accepted 16th July 2015

DOI: 10.1039/c5cp02715b

www.rsc.org/pccp

I. Introduction

Lime (CaO) is a main raw material used in a vast number of natural and industrial processes, including cement, iron and steel, agriculture, food processing, disinfection, water treatment, desulphurization, plastics, glass, sugar refining and pharmaceutical processes, among others. Thus, the calcination of limestone ($CaCO_3$),

$$CaCO_3 \leftrightarrows CaO + CO_2(g) \quad \Delta_r H^\circ = +177.8\ \text{kJ mol}^{-1}, \qquad (1)$$

to obtain lime is probably the most frequently investigated reaction involving the decomposition of a solid reactant. Yet a thorough understanding of the underlying physicochemical mechanisms that govern limestone calcination remains elusive.[1–4] The kinetics of calcination is mainly determined by the calcination temperature, T, the calcination atmosphere and the $CaCO_3$ conversion degree, α (defined as the ratio of the mass of $CaCO_3$ calcined to the initial mass). At a given temperature T, the CO_2 partial pressure at equilibrium is given by:

$$P_{eq}(\text{atm}) \approx 4.083 \times 10^7 \exp(-20\,474/T), \qquad (2)$$

as inferred from thermochemical data.[5–7] If the CO_2 partial pressure in the calcination environment, P, is much smaller than P_{eq}, the rate of $CaCO_3$ conversion is essentially governed by T and can be generally well fitted by an Arrhenius law:[3,4,8]

$$\frac{d\alpha}{dt} = r(T,P)f(\alpha) \qquad (3)$$

$$r(T,P) = A\exp(-E_1/RT)\left(1-\frac{P}{P_{eq}}\right)^{\gamma}, \qquad (4)$$

[a] *Faculty of Physics, University of Seville, Avenida, Reina Mercedes s/n, 41012 Sevilla, Spain. E-mail: jmillan@us.es*
[b] *X-Ray Laboratory (CITIUS), University of Seville, Avenida Reina Mercedes, 4B, 41012 Sevilla, Spain*

where r is the surface reaction rate, $f(\alpha)$ is a mechanistic rate function,[9] A is a pre-exponential term, γ is an empirical exponent of order unity, R = 8.3145 J mol^{-1} K^{-1} is the ideal gas constant and E_1 is a positive activation energy, which is approximately the calcination enthalpy change ($E_1 \approx \Delta_r H^\circ$).[10]

Experimental observations indicate that limestone calcination should occur through a crystallographic transformation involving a topotactical chemical decomposition of $CaCO_3$, yielding an intermediate metastable CaO* phase that subsequently transforms into the stable CaO form.[3,11–16] Accordingly, a reaction mechanism model has recently been proposed consisting of two steps:[17,18]

(a) Chemical decomposition

$$\mathrm{CaCO_3} + \underset{1-\phi}{L} \underset{k_2}{\overset{k_1}{\rightleftharpoons}} \underset{a^*}{\mathrm{CaO}^*} + L(\underset{\phi}{\mathrm{CO_2}})$$

(b) Desorption/structural transformation

$$\underset{a^*}{\mathrm{CaO}^*} + L(\underset{\phi}{\mathrm{CO_2}}) \underset{k_a}{\overset{k_d}{\rightleftharpoons}} \mathrm{CaO} + \underset{1-\phi}{L} + \underset{P}{\mathrm{CO_2}}(\mathrm{g})\,.$$

Here, L represents an active site in the solid where calcination occurs, $L(CO_2)$ denotes a molecule of CO_2 that remains physically adsorbed after chemical decomposition, ϕ is the fraction of active sites filled with adsorbed CO_2, k_i are the reaction rate constants and a^* = exp($\Delta G^*/RT$) is the activity of the metastable CaO* form,[13] where $\Delta G^* = \Delta H^* - T\Delta S^* > 0$ is the free Gibbs energy of formation of the metastable oxide from the stable form. Under the assumption that chemical decomposition is the rate-limiting step (k_1, $k_2 \ll k_d$, k_aP), the reaction rate predicted is:[18]

$$r \approx r_1 = a_1 \exp(-E_1/RT)\left(1 - \frac{P}{P_{\mathrm{eq}}}\right)(1-\phi) \qquad (5)$$

$$1 - \phi \approx \frac{1}{1 + (K_1/a^*)P/P_{\mathrm{eq}}}, \qquad (6)$$

where K_1 = exp($-\Delta_1 G^\circ/RT$), $\Delta_1 G^\circ = \Delta_1 H^\circ - T\Delta_1 S^\circ < 0$ is the standard free energy change of chemical decomposition and the rate constant k_1 is assumed to follow an Arrhenius law with an activation energy E_1 ($k_1 = a_1 \exp(-E_1/RT)$). In the limit of very low CO_2 partial pressure ($P/P_{\mathrm{eq}} \ll 1$) and/or low temperatures ($K_1/a^* = \exp(-(\Delta_1 G^\circ + \Delta G^*)/RT) \ll 1$), the fraction of active sites with adsorbed CO_2 molecules is negligible ($\phi \simeq 0$) and the reaction rate conforms to eqn (4). On the other hand, for P/P_{eq} close to unity and high temperatures ($\exp(-(\Delta_1 G^\circ + \Delta G^*)/RT)(P/P_{\mathrm{eq}}) \gg 1$) it is $\phi \simeq 1 - \exp((\Delta_1 G^\circ + \Delta G^*)/RT)(P_{\mathrm{eq}}/P) \approx 1$. In this limiting situation, CO_2 desorption is hindered and the reaction rate can be written as:

$$r \approx a_1 A_1 A^* \exp\left(-E_{\mathrm{ap}}/RT\right)\left(\frac{P_{\mathrm{eq}}}{P} - 1\right), \qquad (7)$$

where A_1 = exp($-\Delta_1 S^\circ/R$), A^* = exp($-\Delta S^*/R$) and $E_{\mathrm{ap}} = E_1 - \Delta_1 H^\circ - \Delta H^*$. The activation energy under these conditions, E_{ap}, would be negative since the structural transformation is exothermic ($-\Delta H^* < 0$),[16] and the value of E_1 is expected to be of the order of the chemical decomposition enthalpy change, $\Delta_1 H^\circ$. Thus, if P/P_{eq} is high, the reaction rate would conform to eqn (4) with an activation energy $E_1 > 0$ only at low temperatures. As the temperature is increased, the activation energy would decrease with temperature and turn to be negative above a certain critical temperature, T_c. At temperatures above this critical value, the reaction rate markedly decreases with temperature and conforms to eqn (7) in the high temperature limit, as seen from thermogravimetric tests in a recent work.[18] The value of T_c increases as P/P_{eq} is decreased, and for $P/P_{\mathrm{eq}} < 0.6$, the reaction rate adjusts to eqn (4) with a positive activation energy within the whole range of calcination temperatures usually employed in practice.[18]

A. The Ca-looping technology for post-combustion CO_2 capture

The analysis of limestone calcination in environments of high CO_2 partial pressure has gained a great interest in the last years, fueled by the Ca-looping (CaL) technology which has recently emerged for CO_2 capture from coal-fired power plants.[19–21] The multicyclic calcination/carbonation of limestone is at the basis of this potentially low-cost 2nd generation capture technology. Lime particles undergo carbonation at contact with the flue gas in a fluidized bed at temperatures of around 650 °C, after which the partially carbonated solids are circulated into a calciner for CaO regeneration at atmospheric pressure. The main goal of the process is to retrieve CO_2 as a highly-concentrated stream from the calciner reactor. In order not to dilute CO_2 in the calciner reactor, the most suitable method for calcination at high temperatures is to burn coal in the calciner using O_2 (oxy-combustion). Yet calcination under CO_2 at high partial pressures and high temperatures leads to a marked loss of CaO reactivity, which makes it necessary to continuously feed the calciner with a fresh makeup flow of limestone while the deactivated sorbent is purged. According to eqn (2), the minimum temperature for calcination in a pure CO_2 environment at atmospheric pressure (P = 1 atm) would be $T_{\mathrm{cal}} \simeq 895$ °C ($P/P_{\mathrm{eq}} = 1$). Both the carbonator and calciner employed in some 1–2 MWth pilot-scale tests[21,22] and modeled in process simulations[20] are circulating fluidized bed (CFB) reactors operated in the fast fluidization regime, which provide a high heat/mass transfer efficiency for typically short residence times. However, the temperature in the calciner has to be increased to over $T_{\mathrm{cal}} \simeq 930$ °C (or, equivalently, P/P_{eq} decreased below $P/P_{\mathrm{eq}} \simeq 0.6$) for calcination of the makeup flow of natural limestone to be fully achieved in a few minutes.[21–27] This imposes an important energy penalty on the technology, since oxy-combustion requires the additional consumption of fuel and oxygen and generates additional CO_2.[24,25,28–30] The purpose of the present work is to investigate the crystallographic transformation that takes place in the calcination reaction of natural limestone near equilibrium, as affected by a high CO_2 concentration in the calciner environment. To this end, XR diffractograms (XRD) of limestone samples have been continuously recorded *in situ* as the samples undergo calcination for a range of controlled values of P/P_{eq} and temperature. A quantitative analysis of the obtained results will serve to establish a link between the calcination kinetics and the details of the structural transformation.

II. Experimental material and methods

The material tested was a powdered natural limestone of high purity (99.62% $CaCO_3$, SiO_2 < 0.05%, Al_2O_3 < 0.05%, 0.24% MgO, 0.08% Na_2O) from Matagallar quarry (Pedrera, Spain) with an average particle size of 9.5 μm (volume-weighted mean particle size) as measured by laser diffractometry using a Malvern Mastersizer 2000 instrument.

Fig. 1 shows a schematic layout of the experimental setup used in our work. The powder sample of mass around 150 mg was placed over a 1 cm diameter porous ceramic plate. A N_2/CO_2 controlled gas mixture was passed at atmospheric pressure across the powder at a small flow rate (100 cm^3 min^{-1}). By distributing the gas across the sample layer, the gas–solid contacting efficiency was enhanced, which serves to minimize undesired effects of inefficient mass and heat transfer on the reaction rate. Likewise, the small size of the particles allowed us to neglect intra-particle diffusion resistance effects on the reaction rate, which would only be relevant for particles of size larger than 300 μm.[6,31] The powder diffractometer employed (Bruker D8 Advance) was equipped with an Anton Paar XRK 900 high temperature chamber wherein the sample was contained, and a fast response/high sensitivity detector (Bruker Vantec 1) with radial Soller slits, which allowed us to analyze the time evolution of the solid crystal structure as calcination progressed at controlled conditions of temperature and CO_2 partial pressure. The XRK 900 reactor chamber is specifically built for the kinetic analysis of gas–solid reactions up to high temperatures, without any dead volumes to ensure homogeneous filling with the reaction gas. The entire set of the sample and the sample holder rested inside a furnace with a heater designed to guarantee the absence of temperature gradients across the sample. NiCr/NiAl thermocouples placed near the sample holder provided a reliable measurement and control of temperature. *In situ* XRD tests were performed using 60 mm Göbel mirrors (Bruker, Germany) for Cu K_α radiation (0.15405 nm wavelength) and with parallel Johansson geometry in the incident beam. The diffractometer was calibrated mechanically following manufacturer specifications. Corundum, LaB_6 and silicon standards were employed to check resolution and to obtain the instrumental contribution for structural adjustments in a wide range of diffraction angles.

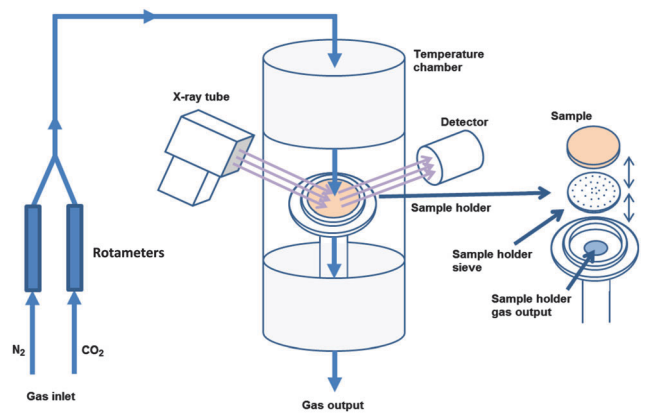

Fig. 1 Schematic layout of the experimental setup.

In each test, the temperature was increased from ambient temperature at 12 °C min^{-1} up to the target calcination temperature, which was kept constant while XRD scans were continuously recorded. The Cu Kα radiation interacted with the sample across a thickness of about 100 μm, which is greater than the particle size in our limestone powder. Thus, the XRD analysis was useful to obtain the time evolution of the $CaCO_3$/CaO weight fraction as calcination progressed. XRD scans of short duration (140 s) were continuously registered in the range 17.5° < 2θ < 39.5° (0.022° per step) to record the main Bragg peaks for calcite and lime with a sufficiently large number of counts in order to analyze the reaction kinetics and the time evolution of the nascent CaO crystallite size. XRD scans were also carried out in a wider range of diffraction angles (18° < 2θ < 115°) in order to carry out a quantitative phase Rietveld analysis aimed at identifying the presence of a metastable CaO* phase during slow calcination, as suggested elsewhere.[3] Calcination tests were performed in a range of CO_2 vol% between 5% and 100% and at temperatures T between 730 °C and 923 °C, so as to yield data series at fixed ratios P/P_{eq} = 0.6, 0.7, 0.8 and 0.9.

III. Results and discussion

A. Calcination kinetics

Fig. 2 illustrates examples of XRD scans recorded during calcination tests in a range of temperatures 857 °C < T < 895 °C and for P/P_{eq} = 0.9. In qualitative agreement with eqn (7) and the existence of a negative activation energy, the diffractograms show that the reaction was significantly hindered for a fixed and high value of P/P_{eq} as the calcination temperature was increased. The induction period that precedes the emergence of the CaO Bragg reflection peaks became also extraordinarily prolonged as the temperature was increased. Thus, for calcination at T = 895 °C (90% CO_2 vol.) the induction period lasted about 45 min, and at T = 903 °C (100% CO_2 vol., P/P_{eq} = 0.9) it took around 70 min. On the other hand, for calcination at 857 °C under 50% CO_2 (P/P_{eq} = 0.9), the reaction started almost immediately after reaching the target temperature. At lower temperatures, calcination had already started when the 1st XRD scan was registered. Once CaO peaks emerge, $CaCO_3$ conversion (α, defined as the ratio of the mass of $CaCO_3$ calcined to its initial mass) can be obtained from a semi-quantitative (S-Q) analysis of the XRD scans as $(1-\alpha)/\alpha = \kappa(M_{CaCO_3}/M_{CaO})(I_{104}/I_{200})$, where $\kappa \simeq 1.39$ is the ratio of calcite to lime corundum numbers, M_{CaCO_3}/M_{CaO} = 100/56 is the ratio of the molecular weights and I_{104}/I_{200} is the ratio of the calcite and lime main reflection peaks intensities. Fig. 3 shows the time evolution of I_{104}/I_{200}, which is seen to decay exponentially with time as calcination progresses ($I_{104}/I_{200} \propto \exp(-\beta t)$). Thus, we may write:

$$\alpha = \frac{1}{1+\exp\left(-\beta\left(t-t_{1/2}\right)\right)} \quad (8)$$

$$\frac{d\alpha}{dt} = \beta\alpha(1-\alpha), \quad (9)$$

where $t_{1/2}$ is the time for half conversion. The time evolutions of $CaCO_3$ conversion obtained for the calcination tests under

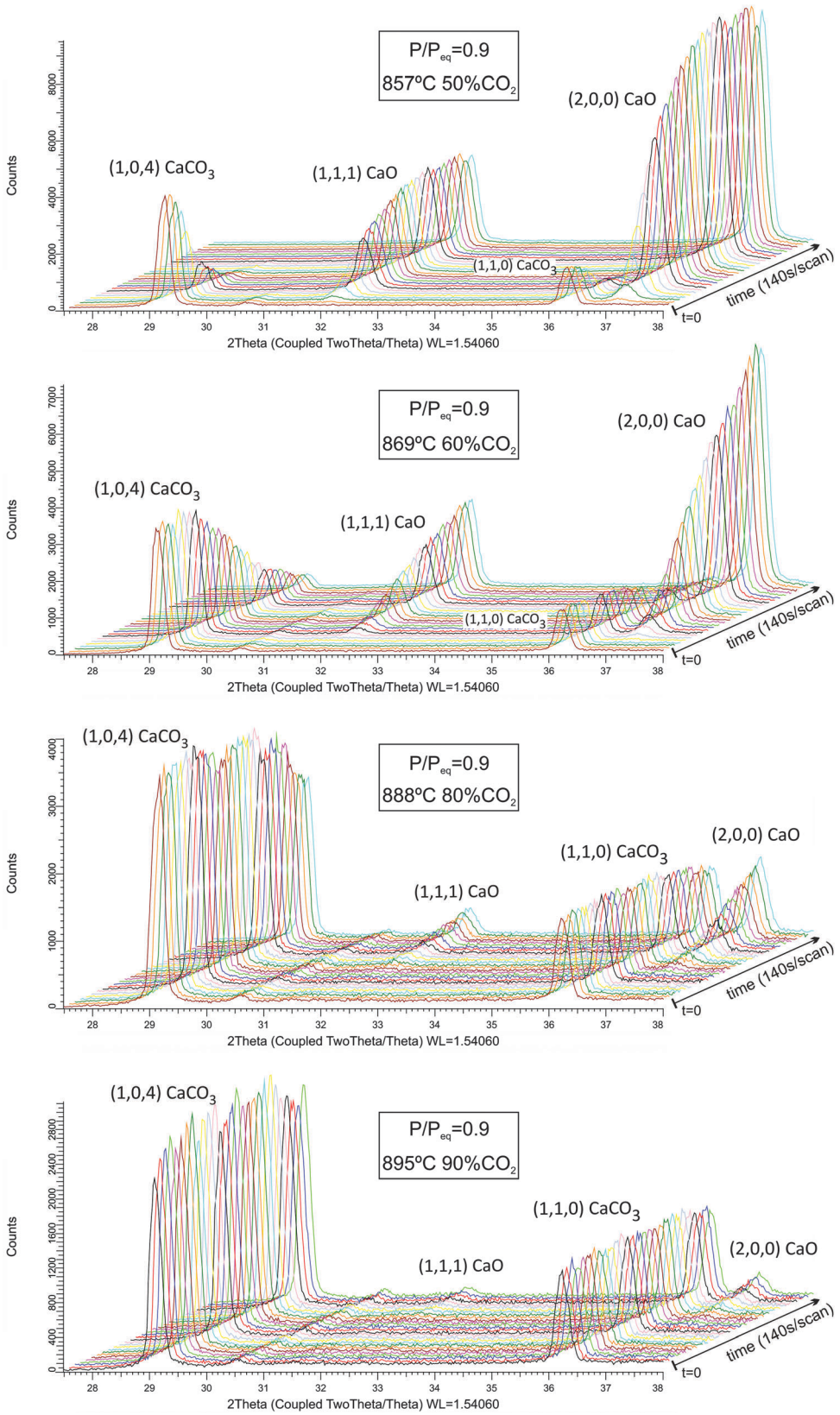

Fig. 2 Diffractograms recorded by *in situ* XRD analysis during calcination of natural limestone at diverse temperatures and CO_2 vol% in the calcination environment, yielding a ratio of the partial CO_2 pressure to equilibrium pressure P/P_{eq} = 0.9. The main Bragg peaks of calcite ($CaCO_3$: Rhombo.H.axes, space group $R\bar{3}c$ (163)) and lime (CaO: cubic, space group $Fm\bar{3}m$ (225)) are indicated.

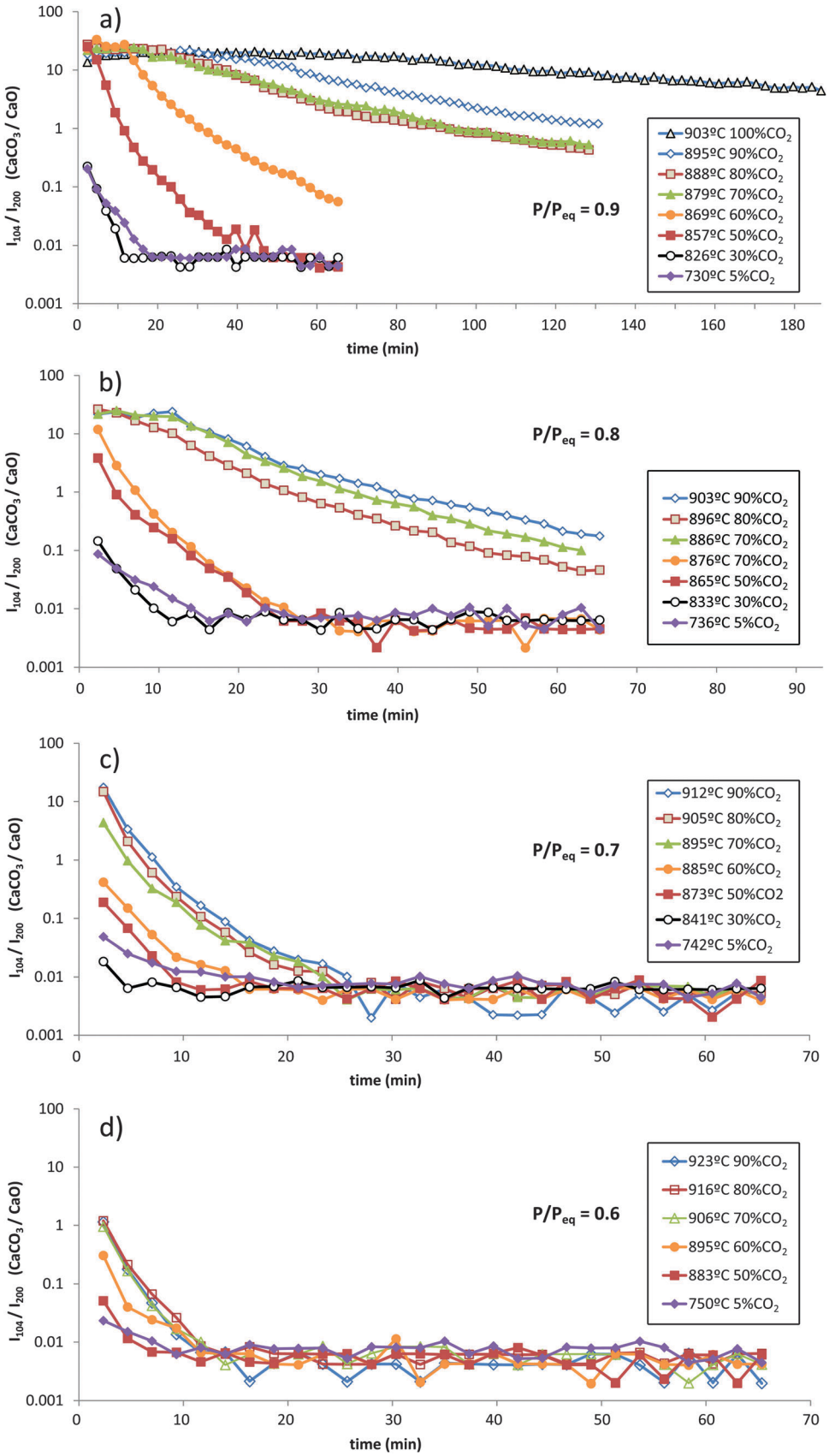

Fig. 3 Ratio of the $CaCO_3$(104) main reflection peak intensity to the CaO(200) main reflection peak intensity during *in situ* calcination tests at diverse temperatures and under different CO_2 vol%. The data series in each graph correspond to the same values of the ratio of CO_2 partial pressure to equilibrium pressure (P/P_{eq}), as indicated. Note the vertical log scale and the diverse horizontal time scales.

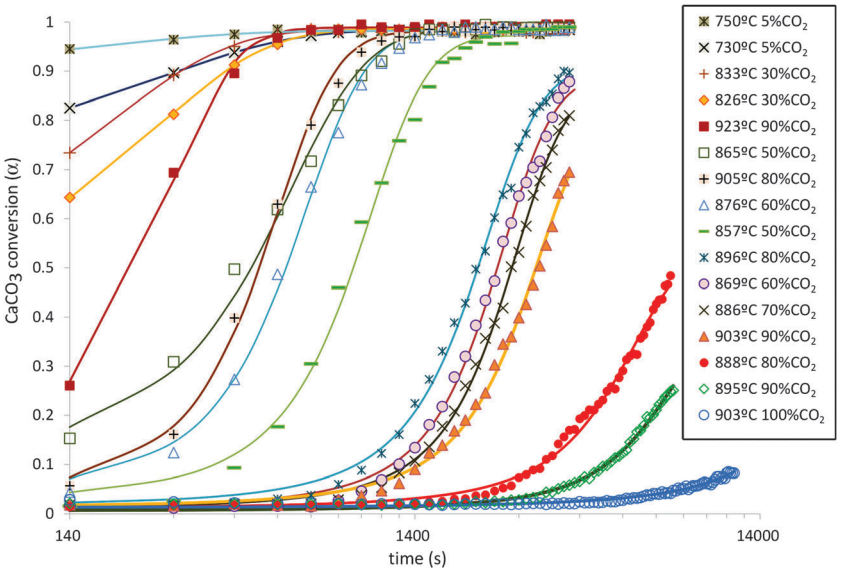

Fig. 4 Time evolution of $CaCO_3$ conversion, obtained from *in situ* XRD semi-quantitative analysis, for calcination tests at the indicated conditions. The solid lines represent the best fits using a sigmoidal function (eqn (8)).

diverse conditions are plotted in Fig. 4. As may be seen, eqn (8) provides a rather good fit to the data. From eqn (9), $\beta = r(T,P)$ can be identified as the reaction rate (eqn (3)), whereas the mechanistic rate function $f(\alpha) = \alpha(1 - \alpha)$ would conform to the Prout–Tompkins model,[9,32] which reflects the common observation of an induction period for heterogeneous reactions before initiation at nucleation sites where reactivity is locally enhanced due, for example, to the presence of structural defects. Accordingly, our experimental results show the existence of an induction period, which becomes extraordinarily prolonged at high temperatures and under CO_2 partial pressures close to the equilibrium pressure, after which calcination proceeds extremely slowly as seen above. As a general observation, we see that the longer the induction period is, the slower calcination occurs afterwards.

Fig. 5 shows data on the calcination reaction rate, $r(T,P) = \beta$, inferred from the *in situ* XRD analysis as a function of temperature and for the diverse values tested of the ratio P/P_{eq}. As predicted by the reaction rate model proposed elsewhere,[18] we observe a change of behavior with temperature which depends on the ratio P/P_{eq}. For $P/P_{eq} \leq 0.7$ and relatively low temperatures, the reaction rate increases with temperature according to an Arrhenius law (eqn (4)) with a positive activation energy of the order of the reaction enthalpy change. In contrast, for $P/P_{eq} \geq 0.8$ and high temperatures, the reaction rate markedly decreases with temperature and is characterized by a negative activation energy. Interestingly, the transition to negative activation energies is seen to occur at a critical value, T_c, which decreases with P/P_{eq}, which is in qualitative agreement with the theoretical expectation. Thus, it is $T_c \simeq 870$ °C for $P/P_{eq} = 0.8$, whereas for $P/P_{eq} = 0.9$ it is $T_c \simeq 830$ °C. The trends shown by the data agree with results obtained by means of thermogravimetric analysis (TGA) reported elsewhere.[18]

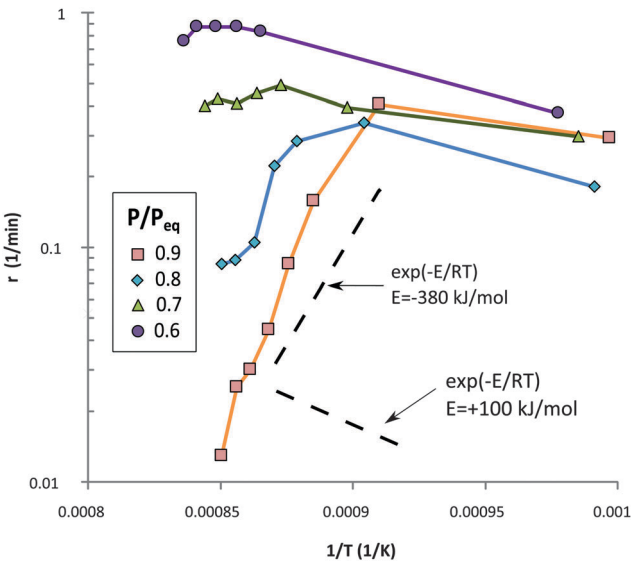

Fig. 5 Reaction rate r as a function of $1/T$ (K) for the calcination tests, as obtained from *in situ* XRD semi-quantitative analysis. The dashed lines show the theoretically predicted trends $r \propto \exp(-E/RT)$ for the values of the activation energy E indicated.

B. The growth of CaO crystallite size

Fig. 6 shows data on the nascent CaO crystallite size (L) as a function of $CaCO_3$ conversion (α), which have been calculated by means of the Le Bail method[33] using the software TOPAS 4.2 (Bruker).[34] The data demonstrate a clear correlation of crystallite size growth with the reaction rate. At the highest ratio of CO_2 partial pressure to equilibrium pressure ($P/P_{eq} = 0.9$), all the data conform to a logarithmic law (L(nm) $\simeq 110 + 25 \ln \alpha$) at calcination temperatures over $T \simeq 870$ °C, involving very slow reaction kinetics. For temperatures above 890 °C (CO_2 vol% > 80%), the data suggest that L would reach a value close to $L_0 \simeq 110$ nm

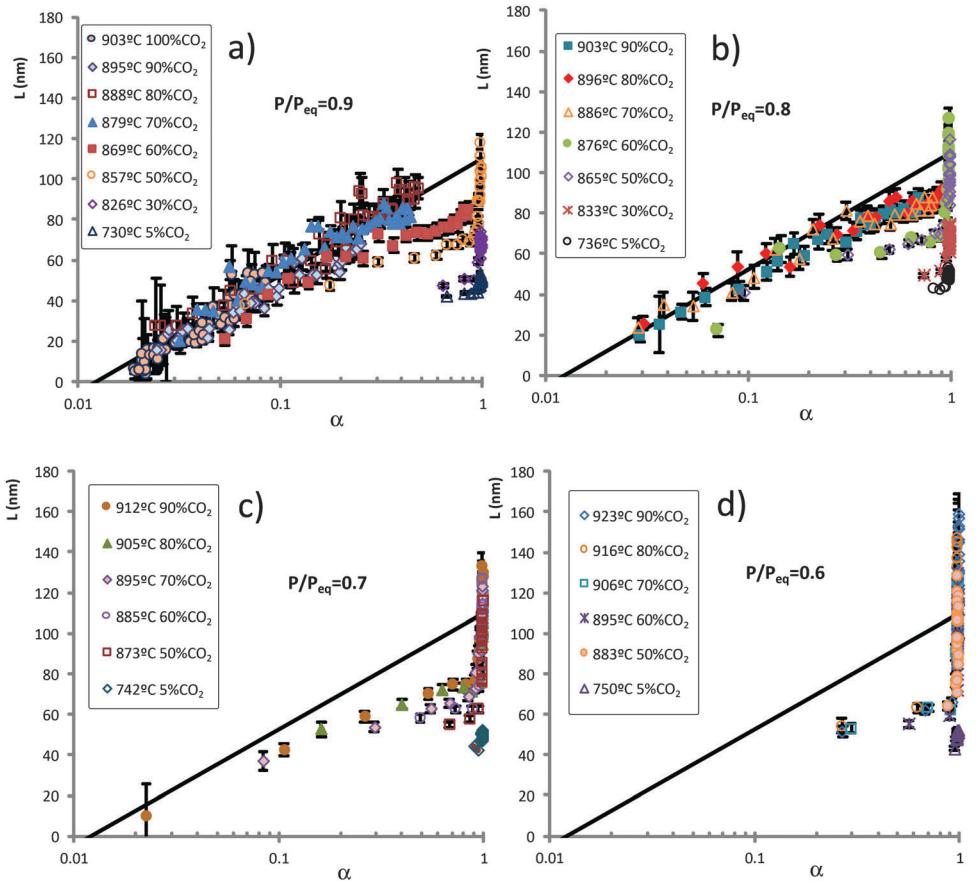

Fig. 6 CaO crystallite size (L) as a function of $CaCO_3$ conversion (α) calculated by Le Bail analysis of *in situ* XRD diffractograms. The calcination tests in each graph were carried out under the indicated conditions and correspond to a given value of P/P_{eq}. The solid line represents the equation $L = 110 + 25 \ln \alpha$ nm.

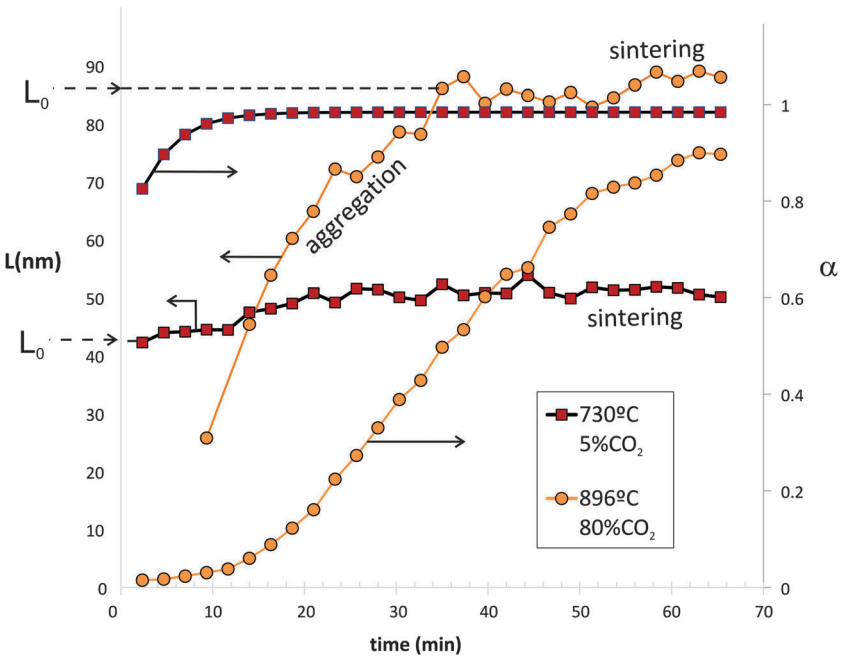

Fig. 7 Time evolution of CaO crystallite size (L) and $CaCO_3$ conversion (α) for calcination conditions yielding slow (896 °C/80% CO_2) and fast (730 °C/5% CO_2) calcination kinetics. The two stages (aggregation and sintering) inferred for the growth of CaO crystallite size are indicated.

for $\alpha = 1$ (Fig. 6a). If $P/P_{eq} = 0.9$ is kept fixed and the calcination temperature is decreased, which speeds up calcination (as seen in the previous section), the growth of CaO crystallites deviates from the logarithmic law trend at an advanced state of conversion. Thus, for $T = 869$ °C (60% CO_2), CaO crystallite size reached a value of $L_0 \simeq 70$ nm for $\alpha \simeq 0.4$, which increased only slightly with conversion afterwards (Fig. 6a). Once conversion had ended ($\alpha = 1$), the size of crystallites continued to grow with time. As the temperature was further decreased or P/P_{eq} was lowered down (the reaction became quicker), the value of L_0 was further decreased. For the fastest calcinations, the logarithmic trend is not observed, since the first XRD pattern registered corresponds already to an advanced state of conversion, giving a value of the crystallite size $L \simeq L_0$ which increases only weakly with conversion.

Fig. 7 shows the time evolution of CaO crystallite size, L, and conversion, α, for two representative cases of slow and fast reaction kinetics. As can be seen, L increased with time at a low rate when the reaction was fast and conversion was finished ($\alpha = 1$) or near to completion. On the other hand, L increased with time at a much larger rate when the reaction was slow (896 °C, 90% CO_2) and conversion was not yet high ($\alpha < 0.5$). After this period (corresponding to the logarithmic dependence of L on α), L reached a value $L = L_0$ that grew with time at a slow rate, similar to the rate of increase observed for quick calcination (730 °C, 5% CO_2). The main difference in the crystallite size evolution between fast and slow calcination kinetics is, thus, the enhanced growth stage that takes place at the beginning of CaO nucleation at high CO_2 partial pressure and at high temperature. The inferred values of L_0 from the data are plotted in Fig. 8a as a function of $1/T$ for the different values of P/P_{eq} tested. The data show that L_0 greatly increases with temperature near equilibrium ($P/P_{eq} \geq 0.8$). L_0 data are plotted in Fig. 8b as a function of the reaction rate, r (min^{-1}). As can be seen, L_0 is well correlated with the reaction rate by means of a power law, $L_0(nm) \simeq 45r^{-0.2}$.

Microscopic observations reported elsewhere on calcination of calcite crystals under vacuum suggest that the growth of CaO crystallites is due to the combination of oriented aggregation of metastable CaO* nanocrystals due to surface attractive forces and sintering afterwards.[3] The time evolution of CaO crystallite size obtained in our work is consistent with this view. Thus, CaO crystallites would evolve in two stages ruled by diverse physical mechanisms, namely aggregation and sintering. In a first stage, when conversion is still low, CaO* nanocrystals would aggregate into larger CaO crystals. The process of aggregation would be driven by the universal van der Waals interaction between solid surfaces, resulting from the attractive forces between the fluctuating dipole moments of the molecules close to the surface. Aggregation would preponderate until conversion reaches a sufficiently high value and the presence of CaO* is reduced. Since the aggregation process would be characterized by a typical time scale, it would not lead to a significant enlargement of CaO crystallite size if calcination is very fast. On the other hand, aggregation would be enhanced for very slow calcination kinetics, as suggested by the correlation between L_0 and the reaction rate (Fig. 8b). Moreover, it is well known that van der Waals attractive

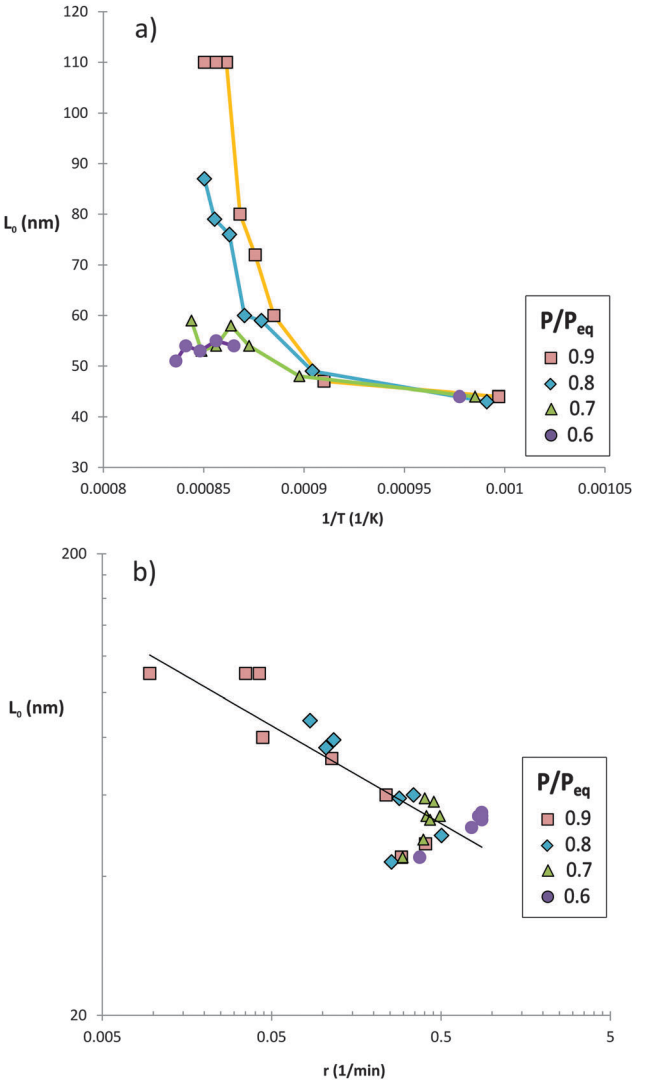

Fig. 8 (a) CaO crystallite size (L_0) at the end of the aggregation stage as a function of $1/T$. (b) The same data plotted *versus* the measured reaction rate r (min^{-1}, Fig. 5). The solid line is the best power law fit ($L_0 \simeq 45r^{-0.2}$).

forces leading to aggregation are intensified by CO_2 adsorption on the surface of the interacting solids.[35] Since CO_2 adsorption is favored at conditions of high temperature and high P/P_{eq},[18] it is foreseeable that aggregation of CaO* nanocrystals would be promoted under these calcination conditions. Once conversion reaches an advanced state, a major part of the crystallographic transformation would be completed and CaO stable crystallites mainly present would continue to grow by sintering. Our results indicate that, compared to aggregation, sintering is less efficient in enlarging crystallite size. This is consistent with the fact that the calcination temperatures are well below the Tamman temperature $T_t \simeq 1170$ °C (the temperature for which diffusion of mobile species in a crystalline lattice leading to sintering becomes significant). Thus, most of the crystallite growth would occur during the aggregation stage taking place at the initial stage of conversion.

It is well known that the CaO carbonation reactivity is directly related to crystallite size; the lower the size, the highest the

reactivity of CaO is.[12,17] Thus, the CO_2 capture efficiency in the CaL technology would be expectedly enhanced at calcination conditions that hinder CaO crystallite growth. According to our study, this goal would be achieved by hampering aggregation of the CaO* nanocrystals during the crystallographic transformation. Arguably, that is a main effect of the addition of inert nanocrystals into the structures of CaO-based synthetic sorbents with enhanced multicyclic stability.[36] Natural dolomite ($CaMg(CO_3)_2$) is a clear example where this mechanism might play a role. Thus, inert MgO nanocrystals would hinder the aggregation of CaO nanocrystals during the crystallographic transformation. As seen in a recently reported study, the multicyclic reactivity of CaO derived from dolomite is greatly enhanced at CaL conditions (involving high CO_2 partial pressure in the calcination environment), compared to CaO derived from limestone.[37,38] Usually, the effect of MgO or inert nano-additives employed in synthetic

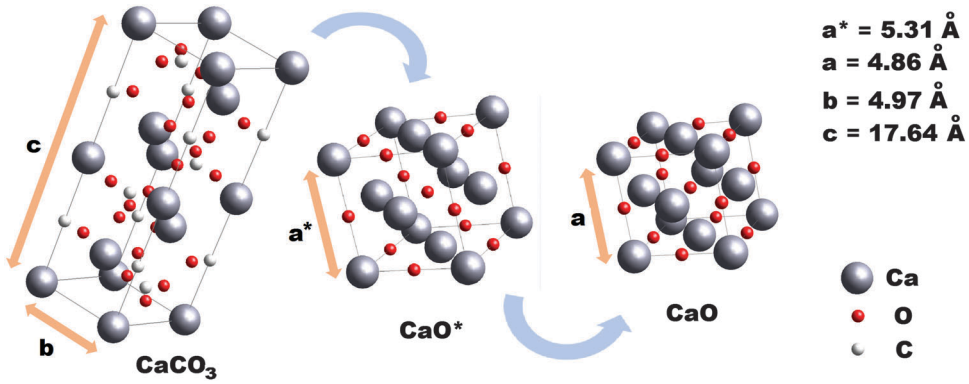

Fig. 9 Hexagonal rhombohedral calcite structure (space group $R\bar{3}c$, 167) yielding during calcination a cubic metastable CaO* structure (space group $Fm\bar{3}m$, 225) as a dilated pseudomorph of lime (same space group as that of CaO*), which appears afterwards. The cell parameters indicated correspond to a temperature of 900 °C.

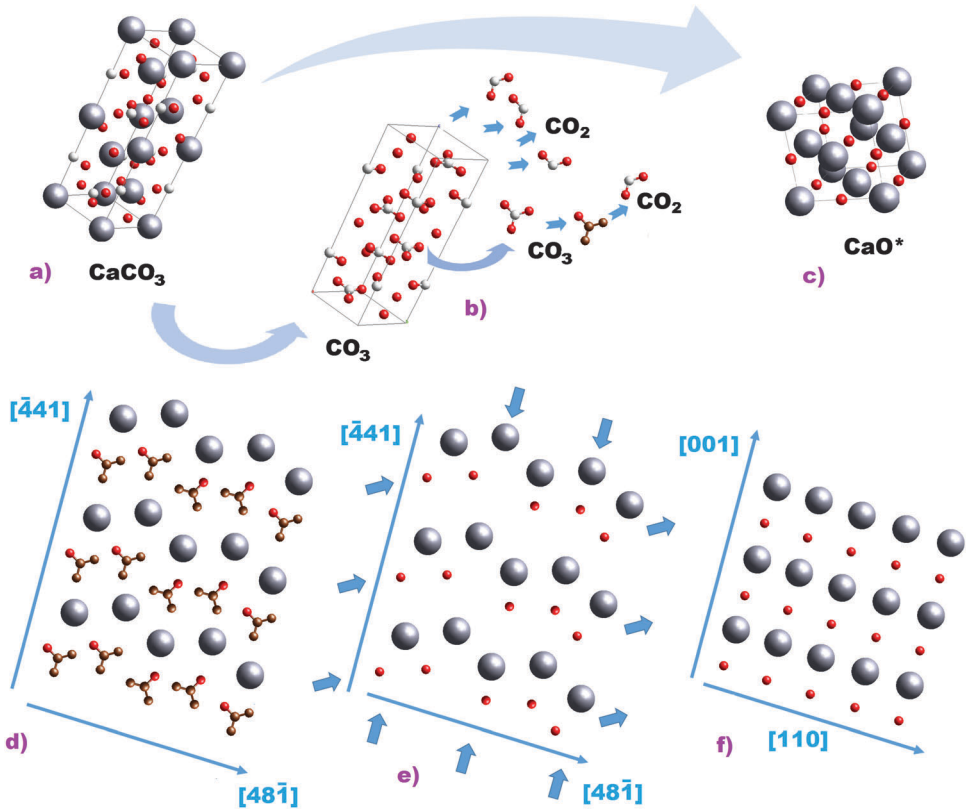

Fig. 10 Schematic representation of the crystallographic evolution of $CaCO_3$ to CaO*. (a) Calcite structure; (b) shows the same structure with hidden Ca atoms and how the CO_2 is released; (c) shows the CaO* resulting structure; (d) and (e) show the (10$\bar{1}$4) calcite plane. In (d), the CO_2 molecule is colored. In (e), CO_2 is released. The arrows mark the direction towards which the remaining Ca and O atoms move; (f) shows the cubic structure of CaO* in the (1$\bar{1}$0) plane.

sorbents[36] is attributed to their higher Tamman temperatures, compared to that of CaO. Yet the Tamman temperature for MgO ($T_t \simeq 1276$ °C) is just slightly above the CaO Tamman temperature.[39] The main difference between MgO and CaO in the CaL process is that the latter suffers a crystallographic transformation in each cycle, whereas the former is inert and remains stable along the cycles. CaO crystallite growth in short calcination times would thus be mainly driven by aggregation during the $CaCO_3$/CaO crystallographic transformation, and not by sintering after calcination is complete. In agreement with this argument, it has been observed that the multicyclic carbonation of dolomite is not improved compared to that of limestone when calcination is carried out under air at reduced temperatures.[37] According to our study, aggregation and sintering of the nascent CaO crystals would not be as relevant at these mild calcination conditions as for calcination under high CO_2 partial pressure.[40]

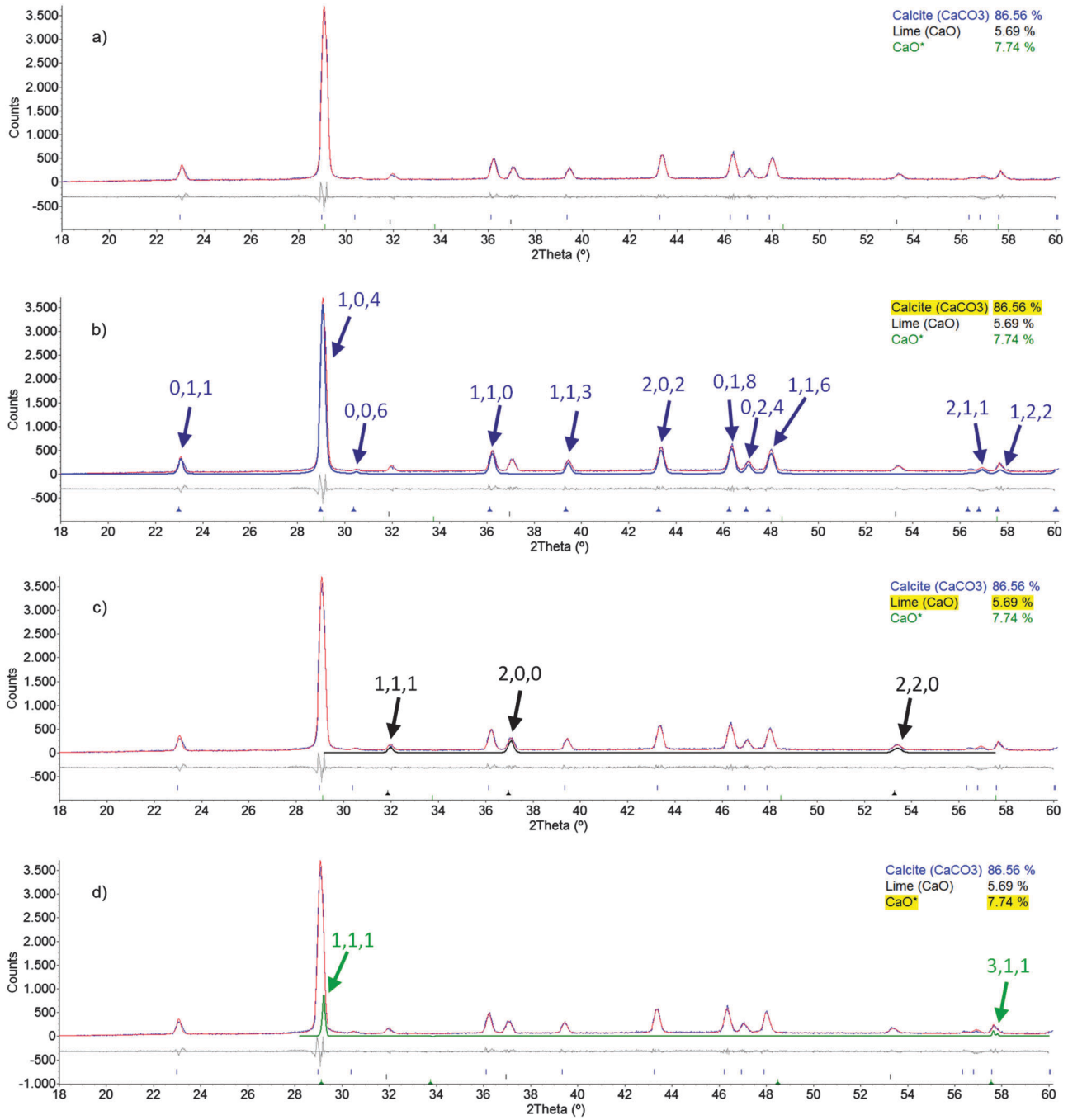

Fig. 11 (a) Experimental diffractogram obtained during *in situ* calcination at 903 °C/100% CO_2 (t = 210 min, blue line) and Rietveld best fit (red). The bottom grey line shows the deviation between the best fit and experimental diffractograms. Figures (b) to (d) show the XRD patterns obtained from the best fit for each one of the three phases present in the indicated wt% (b: calcite, c: lime, d: CaO*).

Thus, the activities of CaO derived from limestone and dolomite decay with the calcination/carbonation cycle number at a similar and relatively small rate.[37]

C. The $CaCO_3$/CaO crystallographic transformation

In situ observations of calcite crystals calcination *in vacuo* by means of transmission electron microscopy coupled with selected area electron diffraction (TEM-SAED) and 2D-XRD analysis[3] have recently evidenced that the calcination of $CaCO_3$ occurs through a solid state topotactic reaction, as was firstly hypothesized by Hyatt *et al.* in 1958.[41] Accordingly, a metastable structure consisting of rod-shaped CaO* nanocrystals is firstly developed on each rhombohedral cleavage face of the calcite pseudomorph.[3] Earlier studies had already shown evidence that limestone calcination should involve a crystallographic transformation.[11–16] Nevertheless, experimental measurements based on *ex situ* XRD conventional analysis could not yield a clear description of the orientation relationships of the metastable CaO* phase. It must be noted that calcination tests in these works were all made at high temperatures, either under vacuum or at very low CO_2 partial pressure (usually air or inert gases). Under these conditions, the structural transformation is extremely fast. On the other hand, the very slow calcination observed in our *in situ* XRD tests at high temperatures and near equilibrium might allow us to identify the footprint and role of the metastable CaO* phase on the reaction progress, by means of a quantitative analysis of the *in situ* XRD scans registered during the transformation.

In order to quantify the presence of an intermediate CaO* metastable structure, an accurate quantitative phase Rietveld analysis of the XRD scans must be performed. To this end, XRD patterns were recorded during *in situ* calcination tests over a wide range of diffraction angles ($18^\circ < 2\theta < 118^\circ$). Even though recording each diffractogram over this wide range of angles takes about 7.5 min, which would preclude in principle an accurate time resolution to investigate the calcination kinetics, these wide scans serve to register the intensity of a large number of reflection peaks, which improves the robustness of the Rietveld analysis results. Moreover, we restricted our study to calcination conditions yielding very slow kinetics ($P/P_{eq} = 0.9$, $T \geq 869$ °C), which expectedly lead to a noticeable presence of CaO*. It must also be remarked that the experimental equipment used allows a rather large number of counts to be registered for each one of the diffraction peaks, as required to carry out a robust quantitative analysis.

According to the crystallographic transformation details that have been inferred from *in situ* calcination observations

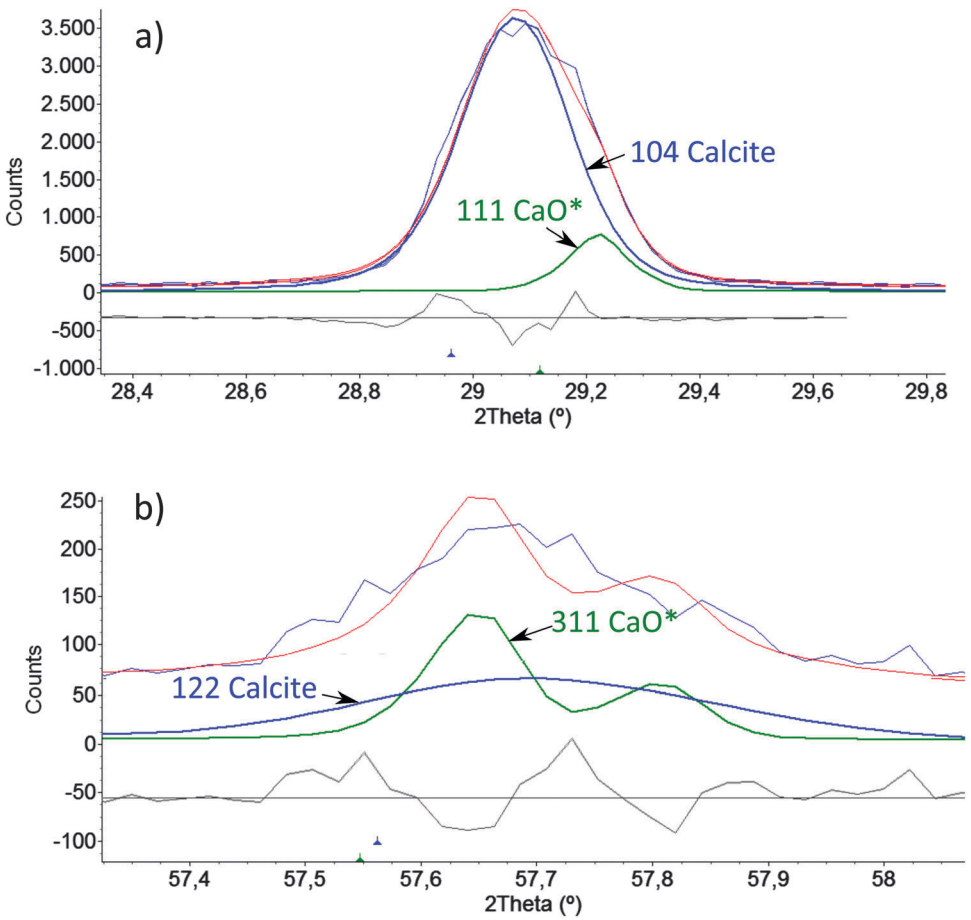

Fig. 12 Expanded regions of the diffractogram shown in Fig. 11, illustrating the contribution of the reflection peaks from the CaO* phase from the best Rietveld fit (red thin line) to the experimental pattern (blue thin line).

under vacuum, we will assume that the CaO* metastable phase stems as a pseudomorph formed from calcite ($CaCO_3$) before the nucleation of lime (CaO).[3] Fig. 9 shows the crystallographic unit cells of the three phases ($CaCO_3$, CaO* and CaO) that would be expectedly involved in the calcination reaction.[3] The hexagonal rhombohedral calcite structure (space group $R\bar{3}c$, 167) yields, at the reaction temperature, the cubic metastable CaO* structure (space group $Fm\bar{3}m$, 225) as a dilated pseudomorph of lime (same space group as that of CaO*), which appears afterwards. The cell parameters for a temperature of 900 °C are, for calcite, b = 4.97 Å and c = 17.64 Å; for CaO*, a^* = 5.31 Å, and for lime, a = 4.86 Å. Fig. 10 schematizes the evolution from calcite to CaO*. In (a), the unit cell of calcite ($CaCO_3$) is depicted with all the atoms. In (b), the cell is shown with only the C and O atoms. Ca atoms have been hidden for the sake of clarity to illustrate the transformation. C and O atoms form CO_3^{2-} ions placed in the same plane. CO_2 is released upon chemical decomposition and escapes from the cell. In (d) and (e), the $(10\bar{1}4)$ calcite plane is displayed, where the Ca^{2+} and CO_3^{2-} ions can be seen, and the marked CO_2 molecules before being released. In (e), the arrows indicate the displacement of the Ca and O atoms remaining in the structure after CO_2 is released, which leads to the metastable CaO* structure. Fig. 10f shows the $(1\bar{1}0)$ plane of the resulting cubic CaO* structure.

The quantitative phase analysis of registered XRD scans has been carried out by means of the Rietveld method,[42] using the software TOPAS 4.2 (Bruker).[34] Zero error (2θ), sample displacement, absorption (cm^{-1}) and the lattice parameters of the phases were allowed to vary to provide the best fits. Importantly, dilation of the structures, as affected by temperature, is considered in the analysis. The background was fitted by a fifth-order Chebyshev polynomial. Lorentz and polarization geometric factors for the measurement configuration were used. For the fittings to be as accurate as possible, the GOF (goodness-of-fit) should be greater than 1, and as close as possible to it.[42] Furthermore, the residual factors (R_{wp} and R_{Bragg}) have to be small for the measurement configuration used.[42] In general, acceptable fitting indicators were obtained in our analysis (GOF ~ 1–1.5, R_{wp} ~ 10, R_{Bragg} ~ 1). The difficulty of early works in identifying a metastable phase[16] from *ex situ* 2D-XRD analysis can be explained on the basis that the CaO* structure yields a main reflection peak (111) at an angle close to the main peak (104) position of the $CaCO_3$ structure. Moreover, calcination tests have been mostly carried under vacuum or air. In these conditions, the structural transformation is extremely fast and the metastable CaO* phase disappears quickly. In our work, the high level of *in situ* XRD technical accuracy achieved, as well as the slow reaction kinetics at conditions close to equilibrium and at high temperatures, enable us to infer the presence of CaO* during the crystallographic transformation, according to the crystallographic structure suggested elsewhere.[3] Fig. 11 shows an example of the Rietveld analysis results on a XRD pattern, which yields the weight% of the three phases involved in the transformation. Expanded regions of the angle intervals comprising the CaO* reflection peaks can be seen in Fig. 12.

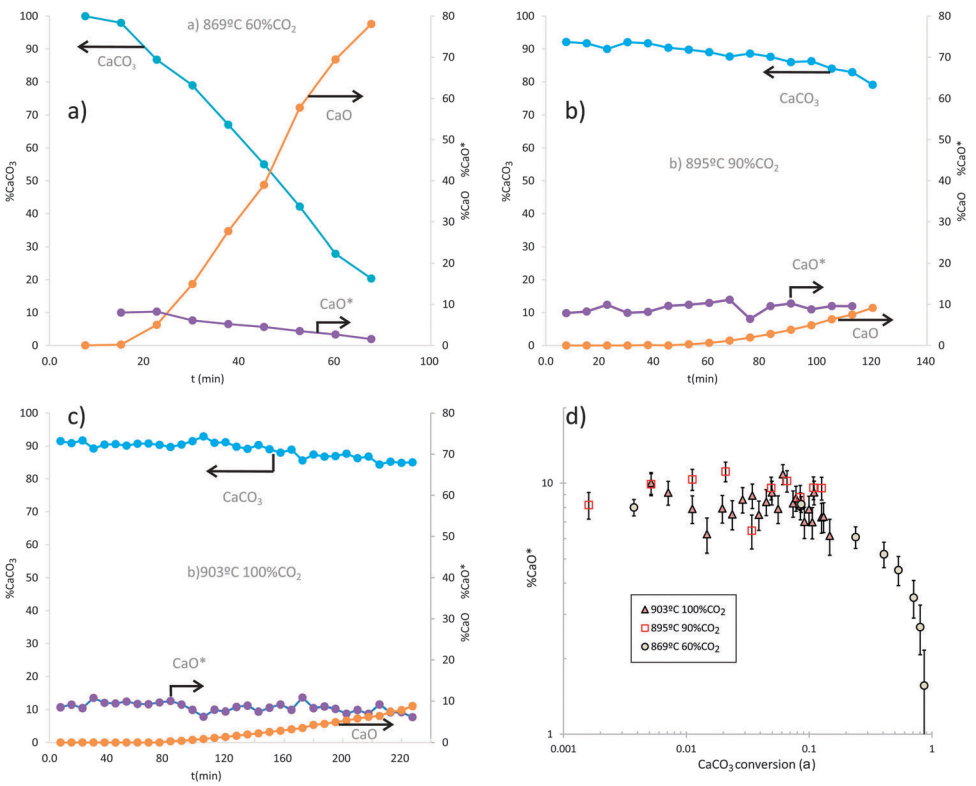

Fig. 13 (a–c) Time evolution of the wt% for the three phases involved in the crystallographic transformation ($CaCO_3$, CaO* and CaO) calculated by means of a Rietveld quantitative analysis for calcination tests near equilibrium (P/P_{eq} = 0.9) under the indicated conditions. (d) CaO* wt% as a function of conversion for the three calcination tests analyzed.

As may be observed, the asymmetry of the main experimental peak (Fig. 12a) is accounted for by the contribution of the (111) CaO* peak to obtain a good fit. Moreover, the experimental reflection intensity between $2\theta \simeq 57.4^\circ$ and 58° needs the contribution of the (311) CaO* peak to get a satisfactory fit.

Fig. 13a–c show time evolution data of the wt% measured for the three phases involved in the crystallographic transformation. At $P/P_{eq} = 0.9$ and high temperatures, the transformation CaO* → CaO is nearly frozen, which allows the detection of a remarkable presence of CaO*, of around 10%, even before the stable CaO crystals nucleate. Thus, chemical decomposition would have occurred during the long induction period preceding the nucleation of CaO, which is hampered by the unfavorable conditions (high temperatures and CO_2 partial pressure near to equilibrium) for the exothermic transformation CaO* →CaO to take place. At these conditions, $CaCO_3$ conversion reaches a small value at the end of the calcination tests at $T = 903$ °C and 895 °C ($\alpha < 0.15$), and CaO* wt% is kept at a high value even after nucleation of the CaO phase. This observation would uphold the argument on aggregation of CaO* nanocrystals as a driving mechanism for CaO crystal growth, which would be relevant during slow calcination as long as the presence of CaO* is kept at a high level. Fig. 13d shows data on the calculated CaO* wt% as a function of conversion. Interestingly, the data adjusts to a common trend independently of the calcination temperature and CO_2 vol%. As long as conversion is small, the wt% of CaO* remains at around 10%, whereas it drops to zero when $CaCO_3$ conversion is above $\alpha \simeq 0.5$, which was reached in the test carried out at 869 °C (60% CO_2). In agreement with the role of CaO* nanocrystal aggregation on CaO crystal growth, the disappearance of the CaO* phase is seen to coincide with the end of enhanced growth of the CaO crystallite size.

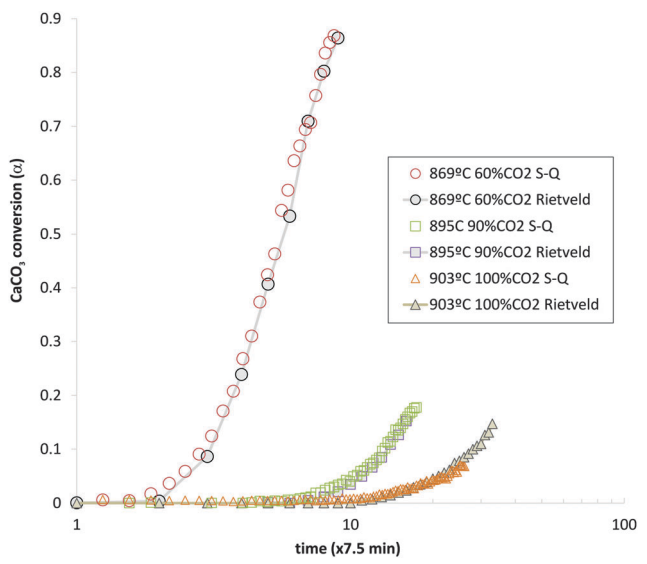

Fig. 14 Time evolution of $CaCO_3$ conversion (α) calculated from a Rietveld quantitative analysis on *in situ* XRD scans registered over a wide range of diffraction angles, and derived from a semi-quantitative analysis using the ratio of intensities of the main $CaCO_3$ and CaO peaks in the scans registered over a reduced window of diffraction angles (Fig. 3a).

$CaCO_3$ conversion data as a function of time directly derived from the Rietveld quantitative analysis are plotted in Fig. 14. The figure also shows conversion data derived from a semi-quantitative analysis (SQ) of the short-time scans (140 s long) registered within a reduced window of diffraction angles (Fig. 3a) and using the ratio of the intensities of the main $CaCO_3$ and CaO peaks. As can be seen, both analyses yield similar conversion data, which supports the validity of the kinetics study described above based on a SQ analysis.

IV. Conclusions

The calcination of limestone under CO_2 becomes extraordinarily slow as the temperature is increased at CO_2 partial pressures near the equilibrium pressure ($P/P_{eq} \lesssim 1$). According to the mechanism proposed elsewhere, the reaction is initiated by the endothermic decomposition of $CaCO_3$, after which CO_2 is desorbed while a metastable CaO* form transforms into the stable CaO phase. If the partial pressure of CO_2 in the calcination environment is very small compared to the equilibrium pressure ($P/P_{eq} \ll 1$), structural transformation and desorption occur extremely rapidly and calcination is just rate-limited by chemical decomposition. On the other hand, CO_2 desorption is hindered at CO_2 partial pressures near to the equilibrium pressure, whereas the activity of the metastable CaO* form decreases as the temperature is increased. As a result, calcination is significantly hampered by an increase of temperature if P/P_{eq} is kept fixed and close to unity. In the present manuscript, the crystallographic $CaCO_3$/CaO transformation at these conditions has been studied in detail by means of *in situ* XRD analysis. A main conclusion is that calcination kinetics, the presence of an intermediate CaO* metastable form and the growth of CaO crystallites are closely related. Near equilibrium ($P/P_{eq} \lesssim 1$), calcination at high temperatures is characterized by a long induction period, after which CaO nucleates at a very slow rate. A steady wt% of CaO* is detected by a significant amount during the induction period and CaO nucleation. Results on the CaO crystallite size suggest that CaO crystallites grow during nucleation at a high rate, as driven by aggregation of CaO* nanocrystals. As conversion reaches an advanced state ($\alpha \gtrsim 0.5$), the wt% of the CaO* phase drops to zero, whereas, at the same time, the growth of the CaO crystallites proceeds at a much slower rate, just driven by sintering. Since the calcination temperatures applied are well below the Tamman temperature, aggregation plays a preponderant role on the final size of the CaO crystallites, which is thus correlated to the reaction rate. Calcination conditions yielding slow kinetics (high P/P_{eq} and high temperature) favor aggregation of the CaO* nanocrystals during a prolonged period, which leads to a large size of the CaO crystallites. On the other hand, if calcination is fast, the metastable CaO* phase is present just for very short times, which limits the growth of CaO crystallites. The fundamental understanding gained in this work on the calcination reaction might be used for practical applications in which the control of the reaction kinetics and CaO crystallite size is relevant.

For example, the Ca-looping technology for CO_2 capture relies on the fast carbonation of CaO derived from limestone calcination under high CO_2 partial pressure. Since CaO carbonation reactivity is inversely correlated to the size of CaO crystallites, CO_2 capture would be enhanced by reducing the strength of surface attractive forces that drive the aggregation of CaO* nanocrystals during the crystallographic $CaCO_3$/CaO transformation, which would be achieved by the insertion of inert nanocrystals in synthetic sorbents or by the presence of inert MgO nanocrystals in dolomite. Thus, our work provides a possible explanation of the enhanced CaO capture capacity displayed by these materials, compared to that of limestone under CaL conditions.

Acknowledgements

This work was supported by the Andalusian Regional Government Junta de Andalucia (contract FQM-5735) and the Spanish Government Agency Ministerio de Economia y Competitividad (contract CTQ2014-52763-C2-2-R). We gratefully acknowledge the X-ray service of the Innovation, Technology and Research Center of the University of Seville (CITIUS).

References

1 R. S. Boynton, *Chemistry and Technology of Lime and Limestone*, Wiley, New York, 1980. For general practical information, the interested reader is recommended to peruse the first edition (1966).
2 B. V. L'vov, L. K. Polzik and V. L. Ugolkov, Decomposition kinetics of calcite: a new approach to the old problem, *Thermochim. Acta*, 2002, **390**(1–2), 5–19.
3 C. Rrodriguez-Navarro, E. Ruiz-Agudo, A. Luque, A. B. Navarro and M. Ortega-Huertas, Thermal decomposition of calcite: Mechanisms of formation and textural evolution of CaO nanocrystals, *Am. Mineral.*, 2009, **94**, 578–593.
4 P. Michele, F. Loic and S. Michel, From the drawbacks of the Arrhenius-$f(\alpha)$ rate equation towards a more general formalism and new models for the kinetic analysis of solid – gas reactions, *Thermochim. Acta*, 2011, **525**(1–2), 93–102.
5 I. Barin, *Thermochemical data of pure substances*, VCH, Weinheim, 1989.
6 F. Garcia-Labiano, A. Abad, L. de Diego, P. Gayan and J. Adanez, Calcination of calcium-based sorbents at pressure in a broad range of CO_2 concentrations, *Chem. Eng. Sci.*, 2002, **57**(13), 2381–2393.
7 B. Stanmore and P. Gilot, Review – calcination and carbonation of limestone during thermal cycling for CO_2 sequestration, *Fuel Process. Technol.*, 2005, **86**(16), 1707–1743.
8 J. M. Criado, M. Gonzalez, J. Malek and A. Ortega, The effect of the CO_2 pressure on the thermal decomposition kinetics of calcium carbonate, *Thermochim. Acta*, 1995, **254**, 121–127.
9 A. Khawam and D. R. Flanagan, Solid-state kinetic models: Basics and mathematical fundamentals, *J. Phys. Chem. B*, 2006, **110**(35), 17315–17328.
10 A. K. Galwey and M. E. Brown, Application of the Arrhenius equation to solid state kinetics: can this be justified?, *Thermochim. Acta*, 2002, **386**(1), 91–98.
11 D. Beruto and A. W. Searcy, Use of the Langmuir method for kinetic studies of decomposition reactions: calcite ($CaCO_3$), *J. Chem. Soc., Faraday Trans. 1*, 1974, **70**, 2145–2153.
12 D. Beruto, A. W. Searcy and M. G. Kim, Calcium oxides of high reactivity, *Nature*, 1976, **5574**, 221–222.
13 A. W. Searcy and D. Beruto, Kinetics of endothermic decomposition reactions. i. steady-state chemical steps, *J. Phys. Chem.*, 1976, **80**(4), 425–429.
14 K. M. Towe, Ultrastructure of calcite decomposition *in vacuo*, *Nature*, 1978, **274**, 239–240.
15 S. Dash, M. Kamruddin, P. Ajikumar, A. Tyagi and B. Raj, Nanocrystalline and metastable phase formation in vacuum thermal decomposition of calcium carbonate, *Thermochim. Acta*, 2000, **363**(1–2), 129–135.
16 D. Beruto, A. W. Searcy and M. G. Kim, Microstructure, kinetic, structure, thermodynamic analysis for calcite decomposition: free-surface and powder bed experiments, *Thermochim. Acta*, 2004, **424**(1–2), 99–109.
17 J. M. Valverde, P. E. Sanchez-Jimenez and L. A. Perez-Maqueda, Limestone calcination nearby equilibrium: Kinetics, CaO crystal structure, sintering and reactivity, *J. Phys. Chem. C*, 2015, **119**(4), 1623–1641.
18 J. M. Valverde, On the negative activation energy for limestone calcination at high temperatures nearby equilibrium, *Chem. Eng. Sci.*, 2015, **132**, 169–177.
19 J. Blamey, E. J. Anthony, J. Wang and P. S. Fennell, The calcium looping cycle for large-scale CO_2 capture, *Prog. Energy Combust. Sci.*, 2010, **36**(2), 260–279.
20 M. C. Romano, Modeling the carbonator of a Ca-looping process for CO_2 capture from power plant flue gas, *Chem. Eng. Sci.*, 2012, **69**, 257–269.
21 B. Arias, M. Diego, J. Abanades, M. Lorenzo, L. Diaz, D. Martinez, J. Alvarez and A. Sanchez-Biezma, Demonstration of steady state CO_2 capture in a 1.7MWth calcium looping pilot, *Int. J. Greenhouse Gas Control*, 2013, **18**, 237–245.
22 J. Ströhle, M. Junk, J. Kremer, A. Galloy and B. Epple, Carbonate looping experiments in a 1MWth pilot plant and model validation, *Fuel*, 2014, **127**, 13–22, Fluidized Bed Combustion and Gasification – CO2 and SO2 capture: Special Issue in Honor of Professor E.J. (Ben) Anthony.
23 A. Charitos, N. Rodriguez, C. Hawthorne, M. Alonso, M. Zieba, B. Arias, G. Kopanakis, G. Scheffknecht and J. C. Abanades, Experimental validation of the Calcium Looping CO_2 capture process with two circulating fluidized bed carbonator reactors, *Ind. Eng. Chem. Res.*, 2011, **50**(16), 9685–9695.
24 A. Martinez, Y. Lara, P. Lisbona and L. M. Romeo, Energy penalty reduction in the calcium looping cycle, *Int. J. Greenhouse Gas Control*, 2012, **7**, 74–81.
25 I. Martinez, G. Grasa, R. Murillo, B. Arias and J. Abanades, Modelling the continuous calcination of $CaCO_3$ in a Ca-looping system, *Chem. Eng. J.*, 2013, **215–216**, 174–181.
26 R. T. Symonds, D. Y. Lu, V. Manovic and E. J. Anthony, Pilot-scale study of CO_2 capture by CaO-based sorbents in the

presence of steam and SO_2, *Ind. Eng. Chem. Res.*, 2012, **51**(21), 7177–7184.
27 A. Coppola, F. Scala, P. Salatino and F. Montagnaro, Fluidized bed calcium looping cycles for CO_2 capture under oxy-firing calcination conditions: part 1. assessment of six limestones, *Chem. Eng. J.*, 2013, **231**, 537–543.
28 N. Rodriguez, M. Alonso, G. Grasa and J. C. Abanades, Heat requirements in a calciner of $CaCO_3$ integrated in a CO_2 capture system using CaO, *Chem. Eng. J.*, 2008, **138**(1–3), 148–154.
29 L. M. Romeo, Y. Lara, P. Lisbona and J. M. Escosa, Optimizing make-up flow in a CO_2 capture system using CaO, *Chem. Eng. J.*, 2009, **147**(2–3), 252–258.
30 A. Martinez, Y. Lara, P. Lisbona and L. M. Romeo, Operation of a cyclonic preheater in the Ca-looping for CO_2 capture, *Environ. Sci. Technol.*, 2013, **47**(19), 11335–11341.
31 G. Grasa, R. Murillo, M. Alonso and J. C. Abanades, Application of the random pore model to the carbonation cyclic reaction, *AIChE J.*, 2009, **55**(5), 1246–1255.
32 M. E. Brown, The Prout-Tompkins rate equation in solid-state kinetics, *Thermochim. Acta*, 1997, **300**(1–2), 93–106.
33 A. Le Bail, Whole powder pattern decomposition methods and applications: A retrospection, *Powder Diffr.*, 2005, **20**, 316–326.
34 A. Bruker, *Topas 4.2 user manual*, Bruker AXS GmbH, Karlsruhe, Germany Search PubMed, 2009.
35 H.-Y. Xie and D. Geldart, Fluidization of FCC powders in the bubble-free regime: effect types of gases and temperature, *Powder Technol.*, 1995, **82**, 269–277.
36 J. M. Valverde, Ca-based synthetic materials with enhanced CO_2 capture efficiency, *J. Mater. Chem. A*, 2013, **1**, 447–468.
37 J. Valverde, P. Sanchez-Jimenez and L. Perez-Maqueda, Ca-looping for postcombustion $\{CO_2\}$ capture: A comparative analysis on the performances of dolomite and limestone, *Appl. Energy*, 2015, **138**, 202–215.
38 A. Coppola, F. Scala, P. Salatino and F. Montagnaro, Fluidized bed calcium looping cycles for CO_2 capture under oxy-firing calcination conditions: Part 2. assessment of dolomite *vs.* limestone, *Chem. Eng. J.*, 2013, **231**, 544–549.
39 A. M. Kierzkowska, R. Pacciani and C. R. Müller, CaO-based CO_2 sorbents: From fundamentals to the development of new, highly effective materials, *ChemSusChem*, 2013, **6**(7), 1130–1148.
40 J. M. Valverde, P. E. Sanchez-Jimenez and L. A. Perez-Maqueda, Calcium-looping for post-combustionCO_2 capture. On the adverse effect of sorbent regeneration under CO_2, *Appl. Energy*, 2014, **126**, 161–171.
41 E. P. Hyatt, I. B. Cutler and M. E. Wadsworth, Calcium carbonate decomposition in carbon dioxide atmosphere, *J. Am. Ceram. Soc.*, 1958, **41**(2), 70–74.
42 *The Rietveld Method. No. 5 in IUCr Monographs on Crystallography*, ed. R.-A. Young, Oxford University Press, New York, 1993.

